

Effect of cubic nonlinearity on auto-parametrically amplified resonant MEMS mass sensor

Wenhua Zhang^{*}, Rajashree Baskaran¹, Kimberly L. Turner

Department of Mechanical and Environmental Engineering, University of California, Engineering II, R2355, Santa Barbara, CA 93106-5070, USA

Received 4 April 2002; accepted 9 August 2002

Abstract

Parametric resonance has been well established in many areas of science, including the stability of ships, the forced motion of a swing and Faraday surface wave patterns on water. We have previously investigated a linear parametrically driven torsional oscillator and along with other groups have mentioned applications including mass sensing, parametric amplification, and others. Here, we thoroughly investigate the design of a highly sensitive mass sensor. The device we use to carry out this study is an in-plane parametrically resonant oscillator. We show that in this configuration, the nonlinearities (electrostatic and mechanical) have a large impact on the dynamic response of the structure. This result is not unique to this oscillator—many MEMS oscillators display nonlinearities of equal importance (including the very common parallel plate actuator). We report the effects of nonlinearity on the behavior of parametric resonance of a micro-machined oscillator. A nonlinear Mathieu equation is used to model this problem. Analytical results show that nonlinearity significantly changes the stability characteristics of parametric resonance. Experimental frequency response around the first parametric resonance is well validated by theoretical analysis. Unlike parametric resonance in the linear case, the jumps (very critical for mass sensor application) from large response to zero happen at additional frequencies other than at the boundary of instability area. The instability area of the first parametric resonance is experimentally mapped. Some important parameters, such as damping co-efficient, cubic stiffness and linear electrostatic stiffness are extracted from the nonlinear response of parametric resonance and agree very well with normal methods.

© 2002 Elsevier Science B.V. All rights reserved.

Keywords: Mass sensor; Chemical sensor; Nonlinearity; Parametric resonance; Damping; Mathieu equation; MEMS

1. Introduction

Parametric resonance has been well established in many areas of science, including the stability of ships [1], the forced motion of a swing [2] and Faraday surface wave patterns on water [3]. We have previously investigated a linear parametrically driven torsional oscillator [4] and along with other groups have mentioned applications including mass sensing [5], parametric amplification [6], and others [7].

For high-precision chemical detection (MEMS nose) [8], mass spectrometry [9], small force detection [10–12], etc. cantilever-based MEMS sensors have been utilized. Micro-scale oscillators are promising due to their small mass and high sensitivity. Many MEMS based mass sensors track shifts in resonant frequency due to changing mass. We have

previously introduced the framework for developing a parametrically driven mass sensor with sensitivity of femtogram (10^{-15} g) mass variation [5]. The presence of cubic mechanical and electrostatic nonlinearity significantly alters the dynamic behavior of the system. Some of these nonlinear effects are beneficial for the use of the oscillator as a mass sensor and a detailed investigation is warranted.

A simple harmonic oscillator (SHO) usually refers to an oscillator that can be modeled by a second-order *constant co-efficient* differential equation with time as the independent variable. In a SHO with 1 d.f., when excited with an external periodic force, the response of the oscillator is restricted to the externally applied frequency. Also, the response is amplified near the resonant frequency and, depending on the damping, the response at all frequencies sufficiently far away from the resonant frequency is minimal. This is not the case when the co-efficients of the second-order system are periodic in time (referred to as parametric oscillators). The dynamics of such oscillators is significantly different from that of the SHO. The response of

^{*} Corresponding author. Tel.: +1-805-893-7849; fax: +1-805-893-8651. E-mail address: whzh@engineering.ucsb.edu (W. Zhang).

¹ Rajashree Baskaran has the same contribution to this paper as Wenhua Zhang.

the oscillator is no longer restricted to the frequency of the externally applied force. In particular, there are excitations of the natural frequency, when excited at certain integer fractions or multiples of the resonant frequency. There is plenty of literature on such systems modeled by Hill's equation and variations including the introductory book by Cartmell [13].

In the case of harmonic oscillators with time-modulated stiffness, a sharp transition between zero response and a large auto-parametric response (sub-harmonic resonance) exists [14]. Since this transition is dependent on system parameters, including the mass of the vibrating oscillators, change in mass can be detected with such a system. In this mass sensor implementation, the minimum detectable mass change can be expressed as [5]:

$$dm = -\frac{k}{4\pi^2 f_0^3} df_0 \quad (1a)$$

where k is the system stiffness and f_0 the natural frequency. The sensitivity of a simple harmonic resonator based mass sensor, such as a cantilever sensor, can be represented as [15–17]:

$$dm = \frac{k}{4\pi^2} \left(\frac{1}{f_0'^2} - \frac{1}{f_0^2} \right) = -\frac{k}{2\pi^2 f_0^3} df_0 \quad (1b)$$

The sensitivity of these two cases is of the same order if the smallest resolvable frequency shift (df_0) due to mass change is the same. However, the sensitivity of a normal cantilever mass sensor is strongly dependent on pressure. The minimum detectable frequency change is inversely proportional to the quality factor [18]:

$$\Delta f = \frac{1}{A} \frac{f_0 k_B T B}{k Q} \quad (2)$$

where A is the amplitude of the oscillation, B the bandwidth, Q the quality factor, T the temperature and k the stiffness of the oscillator. It should be noted that damping cannot be avoided in micro or nano scale [19]. In the case of a parametrically driven oscillator, the sensitivity depends on the transition between zero and large response and the transition can be very sharp. At 7 mTorr, for the case of a parametric torsional mode MEMS oscillator, the transition was observed with an input frequency shift of 0.001 Hz [4], which is the limit of the hardware used (Function generator HP3245A). Because of the sharp transition, with the same configuration, parametrically driven mass sensor can be two orders of magnitude more sensitive than harmonic resonator based mass sensor. In a cantilever mass sensor with dimensions as $22.37 \mu\text{m} \times 2 \mu\text{m} \times 0.5 \mu\text{m}$, the theoretical sensitivity can be $9.65e - 17\text{g}$ [20]. If working in the parametric mode, it can resolve as small a mass change as $3.62e - 19\text{g}$. The sharp transition is a reflection of a sub-harmonic response pitchfork bifurcation in the driving voltage frequency–amplitude parameter space. The occurrence of this bifurcation will be shown to be independent of the ambient pressure (modeled as viscous damping in the dynamics). We have observed this sharp transition at 450 mTorr and higher.

Theoretically, good sensitivity can be achieved even at atmospheric pressure.

In this paper, we describe the motivation for the need to study nonlinear effects and present an introduction to the bulk-micro-machined parametrically actuated mass sensor. We then present the development of its model in the electromechanical domain and present an analytical treatment of the resulting nonlinear Mathieu equations. This analysis is supported with experimental results. The implications of these results on the behavior of the mass sensor are discussed.

2. Device

In this section, we describe the electromechanical system fabricated using the bulk-micro-machining technique SCREAM [21]. The device we have studied is an oscillator, which was designed by Adams et al. [22] for the independent tuning of linear and cubic stiffness terms. A scanning electron micrograph of the oscillator is shown in Fig. 1. The device size is about $500 \mu\text{m} \times 400 \mu\text{m}$. It has two sets of parallel interdigitated comb finger banks on either end of the backbone and two sets of non-interdigitated comb fingers on each side. The four folded beams provide elastic recovery force for the oscillator. The beams, backbone and the fingers are $\sim 2 \mu\text{m}$ wide and $\sim 12 \mu\text{m}$ deep. The backbone is $515 \mu\text{m}$ long and $20 \mu\text{m}$ wide. Each of the four recovery folded beams are $200 \mu\text{m}$ on the long side and $20 \mu\text{m}$ on the short side. Either the interdigitated or the non-interdigitated comb fingers may be used to drive the oscillator. Fig. 2 is a schematic of these comb fingers. This oscillator is used to

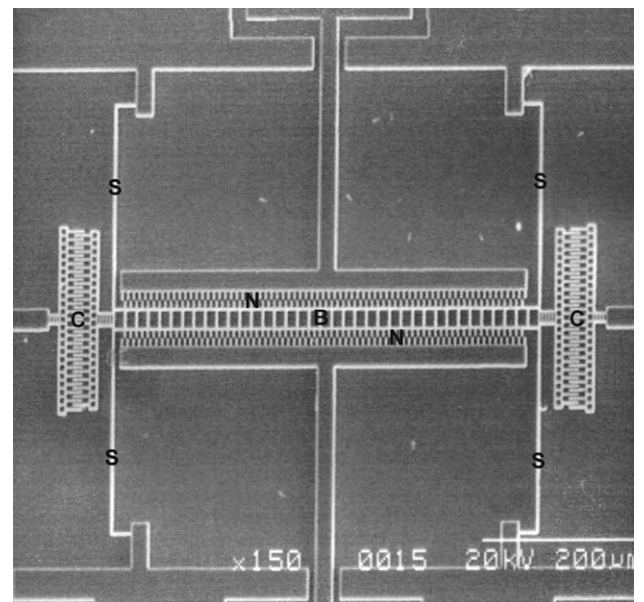


Fig. 1. A scanning electron micrograph of the oscillator. Note the folded beam springs (S), the two sets of interdigitated comb finger banks (C) on both ends of backbone (B) and non-interdigitated comb fingers (N) on each side of backbone (B).

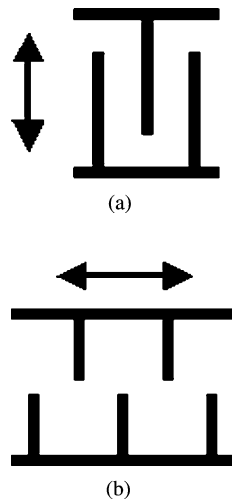


Fig. 2. Schematic of (a) interdigitated comb fingers and (b) non-interdigitated comb fingers that are present in the design of the oscillator shown in Fig. 1.

study the nonlinear effects on the parametric resonance phenomenon. An optimized design (stiffer springs and lesser mass) with a reactive coating specific to the mass sensing application will be used in future versions of the sensor implementations.

The driving force of the non-interdigitated comb finger is proportional to displacement, while the driving force of interdigitated comb fingers is nearly independent of displacement [22]. When a time varying voltage signal is applied to the non-interdigitated fingers, the effective stiffness of the system (mechanical and electrostatic) is dependent on time. At specific frequencies (related to the natural frequency of the device and the strength of the electrostatic drive) and amplitudes of the driving voltage, the sub-harmonics parametric resonance can be excited [4].

3. Theoretical analysis

The approach towards modeling the system is as follows—we use numerical simulation to estimate the mechanical and electrostatic parameters of the oscillator design separately. In the mechanical domain, the details of the spring design predominantly govern the stiffness of the oscillator. A finite element package, ANSYS [23], was used to simulate the spring stiffness. In the electrostatic domain, the configuration of the comb fingers (interdigitated or non-interdigitated) and the dimensions (length of overlap, gap between fingers) govern the electrostatic force generated. The strengths of these electrostatic forces were estimated using a boundary element solver COULOMB [24]. The parameters obtained from these simulations were then used in a single degree of freedom model.

To calculate the stiffness of beams, the device was simplified as shown in Fig. 3, where the dimensions of the folded beams (see Fig. 3(b)) are exactly the same as the

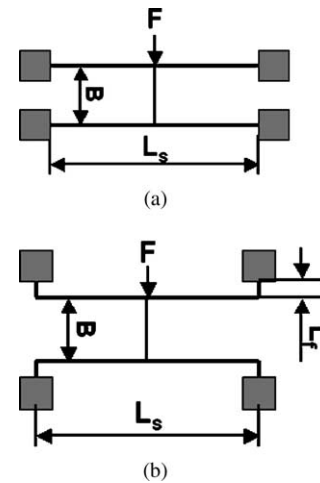


Fig. 3. Simplified models used in estimation of mechanical stiffness using ANSYS: (a) shows the schematic of the fixed–fixed beams and (b) shows the folded beam configuration.

oscillator design and the backbone is represented as a solid beam connecting the two sets of folded beams. Additionally, a fixed–fixed beam (see Fig. 3(a)) with dimensions comparable to the folded beam was used to study the effect of the folding configuration. ANSYS was used to simulate these two models. The dimensions used in the simulations are as follows: length of springs, L_s is 200 μm ; length of folded springs, L_f is 20 μm and backbone equivalent length B is 50 μm . The depth of the features was taken as 12 μm and all the anchor points were assumed fixed in displacement and slope of displacement. The material of the structures was assumed to be single crystal silicon with a young’s modulus of 170 GPa. The results are shown in Fig. 4. At small displacement, the stiffness is close for these two models. But when the displacement is large, their stiffness varies significantly. To get the linear and higher order stiffness, we fit the curve with polynomial functions. The recovery force can be expressed as:

$$F_r(x) = k_1x + k_3x^3 \tag{3}$$

where k_1 is the linear stiffness and k_3 the cubic stiffness.

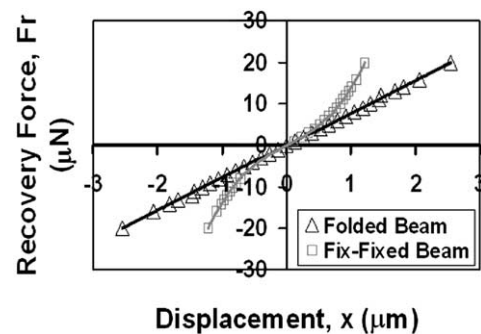


Fig. 4. The results of mechanical stiffness calculation using ANSYS. The curves are fitted with polynomials to extract the linear and cubic stiffness parameters tabulated in Table 1.

Table 1
Simulation results of linear stiffness k_1 and cubic stiffness k_3

	k_1 ($\mu\text{N}/\mu\text{m}$)	k_3 ($\mu\text{N}/\mu\text{m}^3$)
Fixed–fixed spring	8.14	5.8
Folded spring	7.61	$4.4e-2$

The results are shown in Table 1. In the folded beam model, the cubic stiffness is two orders less than with the fixed–fixed model, while the linear stiffness is comparable. Though the cubic stiffness is reduced, it is not negligible in effect on parametric resonance behavior as we show with perturbation analysis and experimental results. We can see from the simulation results in Fig. 4 that the total recovery force grows very fast with displacement for the fixed–fixed beam configuration.

Electrostatic force of the non-interdigitated comb finger was calculated using COULOMB. This boundary element solver can compute the electrostatic forces generated in any configuration of the comb finger spacing. We use the parametric modeling ability in the software to map the electrostatic forces as a function of small displacements of the movable comb fingers relative to the fixed fingers, as shown in Fig. 5. We then define ‘electrostatic stiffness’ as the gradient of this force–displacement curve. By fitting a polynomial curve, we get the linear and cubic electrostatic stiffness, r_1 and r_3 separately (see Table 2). The electrostatic force can be expressed as [22]:

$$F_e(x) = -(r_1x + r_3x^3)V^2 \quad (4)$$

We also show the value of the linear electrostatic stiffness as found by Adams et al. [22] using a combined Finite Element/Boundary Element package HASP. The two results, within 15%, show good correlation.

The oscillator can be simplified as a mass–spring system with electrostatic force as the driving force. Using Newton’s laws, the motion of the device can be described by the following equation:

$$m \frac{d^2x}{dt^2} + c \frac{dx}{dt} + F_r(x) = F_e(t, x) \quad (5)$$

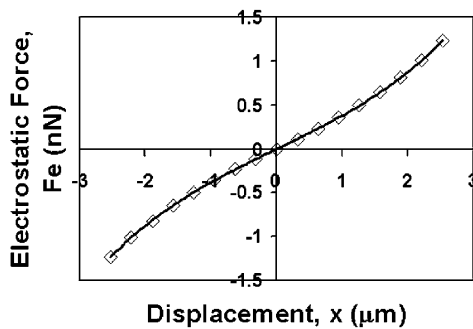


Fig. 5. Numerical results of variation of electrostatic force with displacement of non-interdigitated comb fingers simulated using COULOMB. Linear electrostatic stiffness r_1 and cubic electrostatic stiffness r_3 can be estimated by fitting a cubic polynomial. The results with experimental data comparison are shown in Table 2.

Table 2

Linear electrostatic stiffness r_1 and cubic electrostatic stiffness r_3 calculated using HASP and COULOMB

	r_1 ($\mu\text{N}/(\mu\text{m}/\text{V}^2)$)	r_3 ($\mu\text{N}/(\mu\text{m}^{-3} \text{V}^{-2})$)
HASP	$-3.9e-4$	$-1.4e-5$
COULOMB	$-3.65e-4$	$-1.6e-5$

where x is displacement, m the mass, c the damping coefficient, $F_r(x)$ the elastic recovering force and $F_e(t, x)$ the electrostatic force. Since either interdigitated comb fingers or non-interdigitated comb fingers can be used to drive the oscillator and the dynamic response will be different, these two cases are addressed, respectively.

3.1. Harmonic excitation using interdigitated comb fingers

When an ac voltage signal is applied on the interdigitated comb fingers, F_e is only a function of time, t . F_e can be written as:

$$F_e = F_A \cos(\omega t) \quad (6)$$

Substituting F_e and F_r into Eq. (5) and normalizing it,

$$\frac{d^2x}{d\tau^2} + \alpha \frac{dx}{d\tau} + \beta x + \delta_3 x^3 = f \cos(\tau) \quad (7)$$

where

$$\alpha = \frac{c}{m\omega}, \quad \beta = \frac{k_1}{m\omega^2}, \quad \delta_3 = \frac{k_3}{m\omega^2}, \quad f = \frac{F_A}{m\omega^2}$$

This is a Duffing equation [25]. Considerable work has been done on Duffing equation in MEMS devices to study nonlinear effects on harmonic resonance [22,26–28]. By fitting the frequency response curve, cubic stiffness can be found.

3.2. Parametric resonance excitation using non-interdigitated comb fingers

When the device is driven by non-interdigitated comb fingers, F_e is a function of displacement x and time t . Since the force due to electrostatic interactions has a square dependence on the voltage applied, in order to isolate the parametric effects from harmonic effects, we use a square rooted sinusoidal voltage signal [14]. For the case of square rooted sinusoidal voltage being applied ($V = V_A(1 + \cos(\omega t))^{1/2}$):

$$F_e(x, t) = -(r_1x + r_3x^3)V_A^2(1 + \cos(\omega t)) \quad (8)$$

Substituting F_e and F_r in Eq. (5) and then normalizing it,

$$\frac{d^2x}{d\tau^2} + \alpha \frac{dx}{d\tau} + (\beta + 2\delta \cos 2\tau)x + (\delta_3 + \delta'_3 \cos 2\tau)x^3 = 0 \quad (9)$$

where

$$\alpha = \frac{2c}{m\omega}, \quad \beta = \frac{4(k_1 + r_1 V_A^2)}{m\omega^2}, \quad \delta = \frac{2r_1 V_A^2}{m\omega^2},$$

$$\delta_3 = \frac{4k_3 + 4r_3 V_A^2}{m\omega^2}, \quad \delta'_3 = \frac{4r_3 V_A^2}{m\omega^2}$$

This is a nonlinear Mathieu equation. All the terms in this equation except β (which is of order 1) is of small order. The values of the non-dimensional parameters from simulation at typical voltage amplitude (20 V) and frequency (52 kHz) are $\beta = 1.01$, $\alpha = 1.50e - 3$, $\delta = -1.01e - 2$, $\delta_3 = 5.10e - 3$, $\delta'_3 = -8.75e - 4$

Hence, we can use perturbation methods to study this system.

By assuming $\delta = \varepsilon$, $\beta = \beta_0 + \varepsilon\beta_1$, the equation can be rewritten as a harmonic oscillator with a perturbation (the terms on the right hand side of Eq. (10)).

$$\frac{d^2x}{d\tau^2} + \beta_0 x = \varepsilon \left(-(\beta_1 + 2 \cos 2\tau)x + (\gamma_3 + \gamma'_3 \cos 2\tau)x^3 - \mu \frac{dx}{d\tau} \right) \quad (10)$$

where the terms in Eq. (10) have been scaled with respect to the small term ε ,

$$\gamma_3 = \frac{\delta_3}{\varepsilon}, \quad \gamma'_3 = \frac{\delta'_3}{\varepsilon}, \quad \mu = \frac{\alpha}{\varepsilon} \quad (11)$$

We know that for a linear Mathieu equation, the first-order parametric resonance occurs when the driving frequency is near twice the resonant frequency (here that would correspond to $\beta_0 = 1$). So, we use the ‘method of two variable expansion’ [28] to analyze the equation when driving near the first parametric resonance. The idea of the method is that the expected solution involves two time scales: the time scale of the periodic motions and a slower time scale that modulates the amplitude of the periodic motion. Here, we use the notation that ξ represents stretched time (ωt), and η represents slow-time (εt) [28]:

$$\xi = 2\tau, \quad \eta = \varepsilon t \quad (12)$$

And assuming,

$$x = x_0 + \varepsilon x_1, \quad \beta = 1 + \varepsilon\beta_1 \quad (13)$$

Using two-variable-expansion method, the equation of motion can be rewritten as two equations:

$$4 \frac{\partial^2 x_0}{\partial \xi^2} + x_0 = 0 \quad (14)$$

and

$$4 \frac{\partial^2 x_1}{\partial \xi^2} + x_1 = -4 \frac{\partial^2 x_0}{\partial \xi \partial \eta} - (\beta_1 + 2 \cos \xi)x_0 - (\gamma_3 + \gamma'_3 \cos \xi)x_0^3 - 2\mu \frac{\partial x_0}{\partial \xi} \quad (15)$$

It should be noted that we are working with first-order expansion, neglecting $O(\varepsilon^2)$ terms.

The solution to the harmonic oscillator in x_0 (Eq. (14)) is as follows,

$$x_0 = A(\eta) \cos \left(\frac{1}{2} \xi \right) + B(\eta) \sin \left(\frac{1}{2} \xi \right) \quad (16)$$

Unlike the simple harmonic oscillator case, we have the ‘constants’ A and B varying in slow-time scale. Using Eq. (16) to evaluate the right hand side of the Eq. (15) in x_1 and setting the condition for removal of the resonant terms, yields the slow-flow equations in A and B (the dynamics of A and B in slow-time).

$$\frac{dA}{d\eta} = -\frac{\mu}{2}B + \frac{B}{2}(\beta_1 - 1) + \frac{3B\gamma_3}{8}(A^2 + B^2) - \frac{\gamma'_3 B^3}{4} \quad (17)$$

$$\frac{dB}{d\eta} = -\frac{\mu}{2}A - \frac{A}{2}(\beta_1 + 1) - \frac{3A\gamma_3}{8}(A^2 + B^2) - \frac{\gamma'_3 A^3}{4} \quad (18)$$

The characteristics of these two equations are schematically shown as A – B in β – δ plane (see Fig. 6(a)). The plane can be divided into three areas. In area I, one center exists at

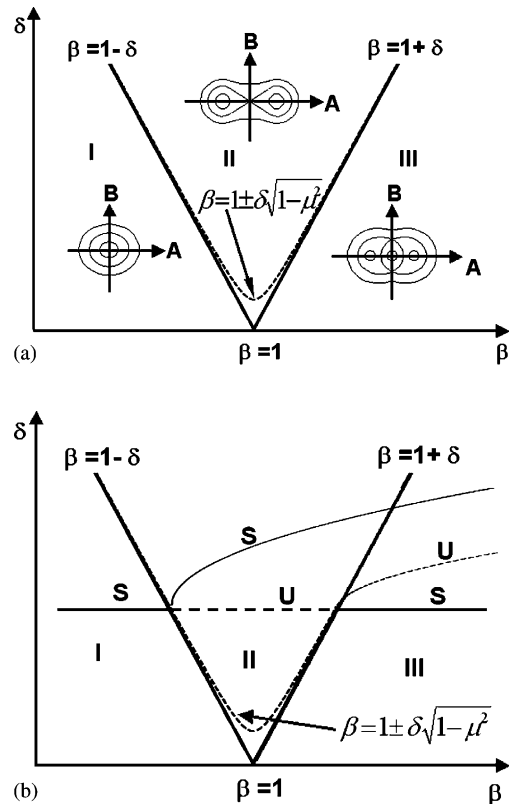


Fig. 6. Dynamic characteristics of nonlinear Mathieu equation in the β – δ plane. $\beta = 1 \pm \delta$ are the transition curves, which divide β – δ plane into area I, II, III. Note the damping effects on transition curves ($\beta = 1 \pm \delta\sqrt{1 - \mu^2}$) in Fig. 6(a). The number of stable points change in each area—one center at $(0, 0)$ in area I, two centers at $(\pm a_1, 0)$, and one saddle at $(0, 0)$ in area II, three centers at $(\pm a_2, 0)$ and $(0, 0)$ and two saddles at $(0, \pm b)$ in area III. Fig. 3(b) shows how the positions of the stable (dark trace) and unstable (broken trace) points vary as β and δ are varied quasi-statically.

(0, 0) which means only one stable trivial solution exists in the area. In area II, there are two centers at $(\pm a_1, 0)$ and one saddle at (0, 0), corresponding to one stable non-trivial solution and one unstable trivial solution. In area III, there are two centers at $(\pm a_2, 0)$, two saddles at (0, $\pm b$) and one center at (0, 0), corresponding to one stable non-trivial solution, one unstable non-trivial solution and one stable trivial solution.

It is convenient to study Eqs. (17) and (18) in polar system. Assuming

$$A = R \cos \theta, \quad B = R \sin \theta \tag{19}$$

We get

$$\frac{dR}{d\eta} = -\frac{\mu R}{2} - \frac{R}{2} \left(1 + \frac{\gamma'_3 R^2}{4} \right) \sin(2\theta) \tag{20}$$

$$\frac{d\theta}{d\eta} = -\frac{\beta_1}{2} - \frac{3\gamma_3 R^2}{8} - \left(\frac{\gamma'_3}{4} R^2 + \frac{1}{2} \right) \cos(2\theta) \tag{21}$$

The fixed points (R^*, θ^*) of these coupled equations are obtained by setting $(dR/d\eta) = 0$ and $(d\theta/d\eta) = 0$. This yields:

$$\sin(2\theta^*) = -\frac{4\mu}{4 + \gamma'_3 R^{*2}} \tag{22}$$

and

$$R^{*2} = -\frac{4}{3} \left[\frac{\beta_1 + \cos(2\theta^*)}{(\gamma_3 + (2/3)\gamma'_3 \cos(2\theta^*))} \right] \tag{23}$$

Fixed points (centers and saddles) occur when there is a real value for R^* and to facilitate the discussion, we define a new variable,

$$\gamma_{3\text{eff}} \gamma_3 + \frac{2\gamma'_3}{3} \cos(2\theta) \tag{24}$$

Inserting $\gamma_3 = (\delta_3/\varepsilon)$ and $\gamma'_3 = (\delta'_3/\varepsilon)$ into Eq. (24) yields:

$$\gamma_{3\text{eff}} = \frac{2k_3}{r_1 V_A^2} + \frac{r_3}{r_1} \left(2 + \frac{4}{3} \cos(2\theta^*) \right) \tag{25}$$

where $\gamma_{3\text{eff}}$ is the effective nonlinearity parameter of the system, a sum of contributions from cubic mechanical stiffness, (fixed for a particular beam design) and voltage dependent cubic electrostatic stiffness. Looking at Eq. (9), it might be tempting to conclude that the effective contributions of the mechanical and electrostatic cubic stiffness will be just a linear sum of k_3 and $r_3 V_A^2$.

The detailed analysis presented above shows that the effective contribution is subtle and depends on the linear electrostatic stiffness r_1 and the response of the oscillator itself (the $\cos(2\theta^*)$ term). In the current design, the mechanical cubic stiffness k_3 is positive and the electrostatic cubic stiffness r_3 is negative. Hence by varying the applied voltage, V_A , we can change the sign of the effective cubic stiffness. Fig. 7 is the variation of $\gamma_{3\text{eff}}$ with the input voltage for the device under study. The effect of the sign of the effective cubic stiffness is presented in detail in Section 5.

For clarity of discussion, we present the influence of damping and nonlinear terms on parametric resonance separately.

3.2.1. Effect of damping (assuming no cubic nonlinearity)
Eqs. (17) and (18) can be simplified as:

$$\frac{dA}{d\eta} = -\frac{1}{2}(\mu)B + \frac{1}{2}(B)(\beta_1 - 1) \tag{26}$$

$$\frac{dB}{d\eta} = -\frac{1}{2}(\mu)A - \frac{1}{2}(A)(\beta_1 + 1) \tag{27}$$

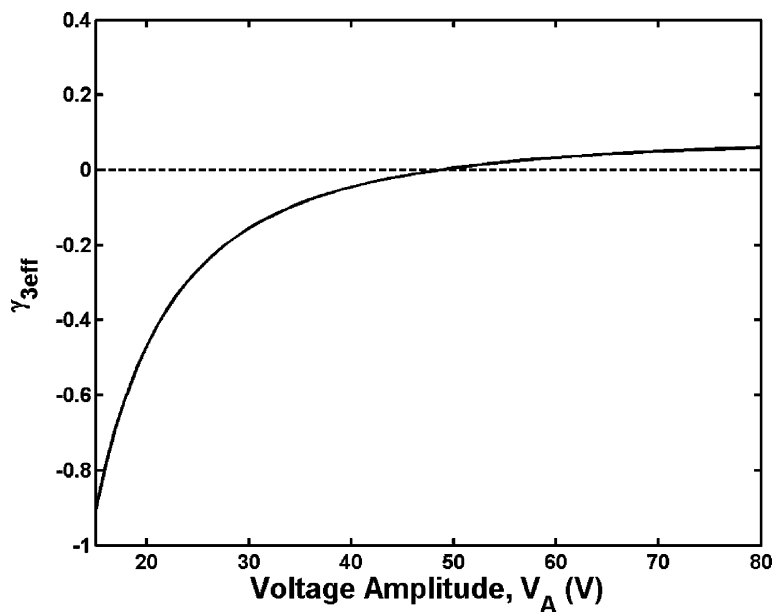


Fig. 7. The effective nonlinear parameter as a function of the driving voltage amplitude V_A for the spring and electrostatic comb finger design of the oscillator studied in this paper. Note that the sign of effective nonlinear parameter can be changed at large voltage amplitude.

Eqs. (26) and (27) are called the slow-flow equations. These are coupled linear first-order differential equation that can be easily solved. The slow-time dynamics of the variable A and B distinguish the resonant and non-resonant regions. The transition of the real part of the eigenvalues from positive (exponentially growing solution) to negative (exponentially decaying solution), corresponds to the transition curve from unstable to stable areas in the first parametric resonance stability plot [28]:

$$\beta = 1 \pm \varepsilon \sqrt{1 - \mu^2} = 1 \pm \sqrt{\varepsilon^2 - \alpha^2} \quad (28)$$

Fig. 6 also shows the effects of damping on parametric resonance. The presence of damping limits the occurrence of the parametric resonance to above certain critical input voltage amplitude. By substituting $\alpha = (2c/m\omega)$, $\beta = (4(k_1 + r_1 V_A^2)/m\omega^2)$, $\varepsilon = \delta = (2r_1 V_A^2/m\omega^2)$, we can find the equation of boundary curve in $V_A - f$ plane and get the critical input voltage.

3.2.2. Effect of cubic nonlinearity (assuming no damping)

We look at the slow-flow equations in polar coordinates here, assuming damping co-efficient $\mu = 0$.

$$\frac{dR}{d\eta} = -\frac{1}{2}(R) \sin(2\theta) \quad (29)$$

$$\frac{d\theta}{d\eta} = -\frac{\beta_1}{2} - \frac{3\gamma_{3\text{eff}}R^2}{8} - \frac{1}{2} \cos(2\theta) \quad (30)$$

We study the equilibrium (fixed) points of the slow-flow variable (R^*, θ^*) and analyze their stability characteristics. The equilibrium points are when the right hand side of the above equations is identically zero. For non-trivial solutions

of R , equilibrium points are

$$\theta^* = 0, \quad \frac{\pi}{2}, \quad \pi, \quad \frac{3\pi}{2}$$

and

$$R^{*2} = -\frac{4}{3\gamma_{3\text{eff}}}(\beta_1 + \cos(2\theta^*)) \quad (31)$$

Let us assume the effective nonlinearity parameter $\gamma_{3\text{eff}} < 0$. In the case of $\theta^* = 0$ and π , $R^{*2} = -(4/3\gamma_{3\text{eff}})(\beta_1 + 1)$, non-trivial solutions require $\beta_1 > -1$. When $\theta^* = \pi/2$ and $3\pi/2$, $R^{*2} = -(4/3\gamma_{3\text{eff}})(\beta_1 - 1)$, non-trivial solutions exist only for $\beta_1 > 1$. The characteristics of Eq. (31) are schematically shown in Fig. 6(b). Since $\beta_1 = \pm 1$ corresponds to transition curves from stable to unstable areas in $\beta - \delta$ plane, bifurcation occurs when we quasi-statically vary frequency of the input voltage across the transition curve. The growth of R^* with respect to β in different areas is schematically shown in Fig. 6(b), where solid line represents stable solution and dashed line represents unstable solution. The solutions in different cases are reflected in the results presented in $A - B$ plane (Fig. 6(a)).

4. Experimental results

A multi-dimensional MEMS motion characterization suite is used to measure the in-plane movement of the device [29]. The schematic setup is shown in Fig. 8. The device is placed in a vacuum chamber, where the pressure can be pumped to as low as 7 mTorr. The Laser Doppler Vibrometer with built in controllers and sensor heads (Polytec, OFV-

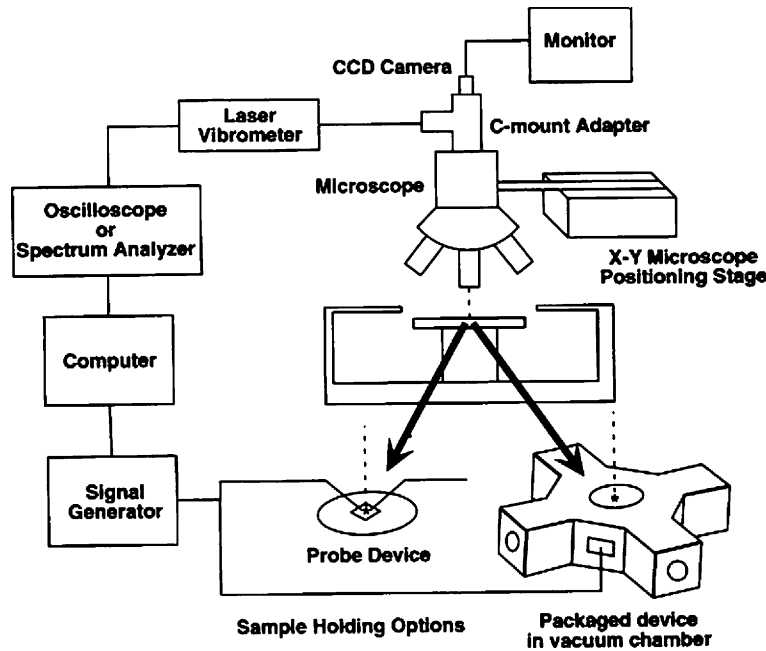


Fig. 8. Schematic of characterization suite used to test the MEMS oscillator. For the results presented in this paper, we used a vacuum chamber with a pressure of ~ 7 mTorr.

3001, and OFV-511) uses a 633 nm wavelength, 205 mm cavity length Helium–Neon laser. The principle of measurement is optical interferometry. It is a heterodyne interferometer, meaning the velocity magnitude as well as the direction is determined by use of an additional Bragg cell [30]. A voltage source (HP3245A) is used for input voltage signal generation and the displacement and velocity outputs from the Vibrometer were recorded and analyzed with a HP Spectrum Analyzer (HP89470A) and Tektronics Oscilloscope (TDS 420 A).

To obtain natural frequency and quality factor (defined as the ratio between the frequency of the peak amplitude and the band width of the frequency response at half power points), an ac voltage signal (~ 20 V) is applied on the interdigitated comb fingers. For this design, a driving voltage of 20 V applied to the interdigitated comb fingers results in an amplitude of motion less than 1 μm , which can be adequately modeled with a linear stiffness. The position independent actuation of the interdigitated fingers is used in order to avoid parametric excitation effects. At 7 mTorr, the natural resonance frequency is 26.48 kHz and quality factor is 640 (see Fig. 9).

A larger electrical signal (~ 60 V) is applied on the interdigitated comb finger to study the nonlinear behavior of the device. The motion of the device under this driving voltage is greater than 2.5 μm . Its frequency response follows that of a Duffing equation response (see Fig. 10) [25,27]. By fitting the curve with the solution to the Duffing equation, cubic stiffness can be obtained [26,27]. At 7 mTorr, k_3 is found to be $0.030 \mu\text{N}/\mu\text{m}^3$, which compares well with FEM results (see Table 1).

To avoid coupling between harmonic resonance and parametric resonance, a square root sinusoidal ac voltage signal is applied to the non-interdigitated comb fingers [14]. The device displays parametric resonance when excited with a frequency around twice the natural frequency. The time-scale growth of the response (Fig. 11(b)) is quite different

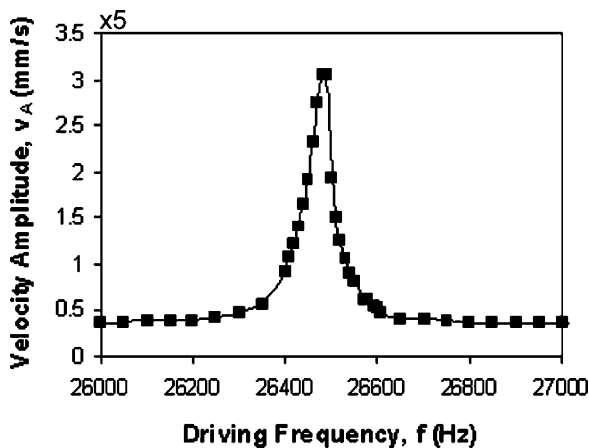


Fig. 9. The oscillator’s frequency response curve when excited with the interdigitated comb fingers with a small ac voltage ($V_A = 20$ V). At small amplitudes of motion, the oscillator is essentially linear and the linear stiffness to mass ratio (natural frequency) and the damping co-efficient (Q —the quality factor) values are extracted from this data.

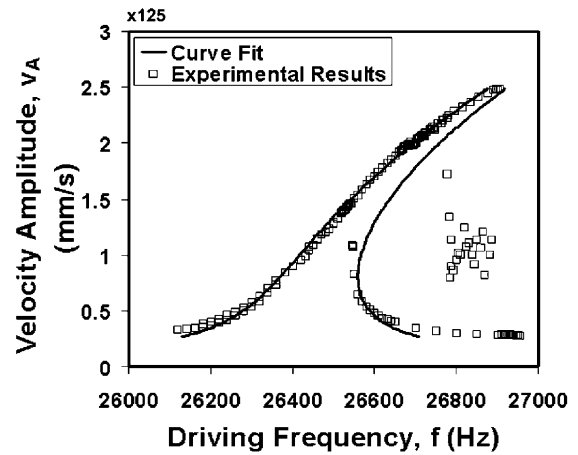
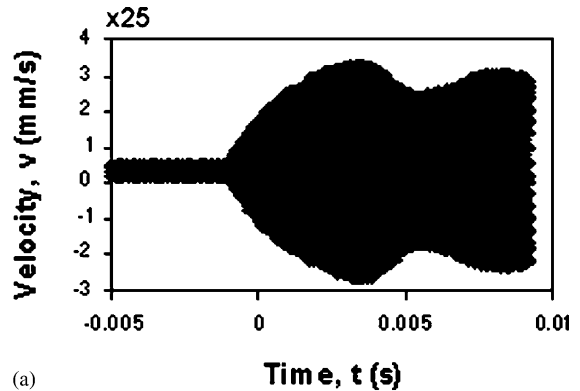
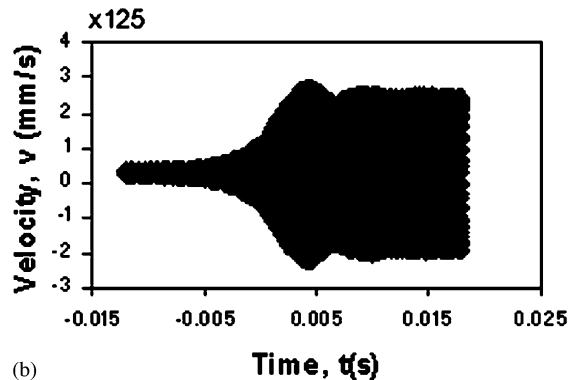


Fig. 10. The oscillator’s frequency response curve when excited with the interdigitated comb fingers with a high voltage ($V_A = 60$ V). This isolates the effect of mechanical cubic nonlinearity with that of the electrostatic nonlinearity since the latter arises only when driven by non-interdigitated comb drives. The experimental data is represented by squares and the smooth line is the fit using solution to a Duffing equation. The mechanical cubic stiffness extracted from this curve is $k_3 = 0.030 \mu\text{N}/\mu\text{m}^3$.



(a)



(b)

Fig. 11. Comparison of time–response of oscillator velocity when excited at (a) harmonic resonance (driving voltage 60 V) and (b) first-order parametric resonance (driving voltage 20 V). The contrasting feature here is that the latter has an exponential envelope of growth of the sinusoidal amplitude, while the former has linear growth.

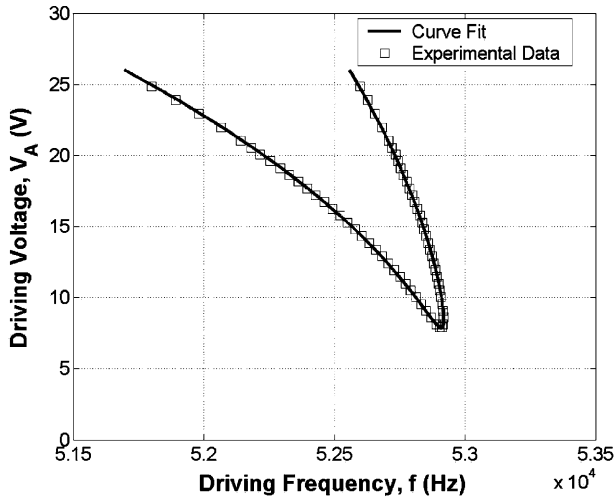


Fig. 12. Map of the first parametric resonance transition curve in $V_A - f$ plane (driving voltage amplitude–driving frequency) at 7 mTorr. The squares represent experimental data. The equation of the curve fit is derived from nonlinear Mathieu Eq. (28). The Q (quality factor) and linear electrostatic stiffness r_1 can be found by fitting this curve.

from that of a harmonic resonance (see Fig. 11(a)). When excited from a non-resonant point in the input voltage–frequency space to a resonant region, parametric resonance grows exponentially with time while harmonic resonance grows linearly, as shown in Fig. 11(a) and (b).

The first parametric resonance instability area is mapped by sweeping frequency and amplitude of the input voltage signal (see Fig. 12). By fitting this data at the transition curve with the analytical result (Eq. (28)) in $V_A - f$ format, the linear electrostatic force co-efficient and Q factor can be extracted. Linear electrostatic force co-efficient ($r_1 = -3.67e-4 \mu\text{N}/(\mu\text{m}/\text{V}^2)$) is in good agreement with the Boundary Element simulations value of $r_1 = -3.65e-4 \mu\text{N}/(\mu\text{m}/\text{V}^2)$. The quality factor Q ($Q = 671$) matches with the result obtained from small signal harmonic frequency response ($Q = 640$).

Fig. 13 is the response of the device when excited with frequencies corresponding to the first parametric resonance at $V_A = 20$ V. The frequency is swept from low to high (up) and high to low (down). Different step sizes are used in the sweeping. When sweeping frequency down, the jump from small amplitude to large amplitude response occurs around 52.7 kHz. This corresponds to the moving quasi-statically from region III to region II in Fig. 6(b). When sweeping the frequency up, the jump (from large amplitude response to zero response) happens at about 53.7 kHz. This corresponds to moving from region II to region III in Fig. 6(b). In region III, there are two possible stable states of response of the system. Initial conditions determine which one of the two will be preferred. This jumping point depends on the step size of frequency. The smaller the step size, the larger is the jumping frequency (points S and R). Changing the frequency quasi-statically introduces a perturbation in the system, which alters the initial state of the system. We

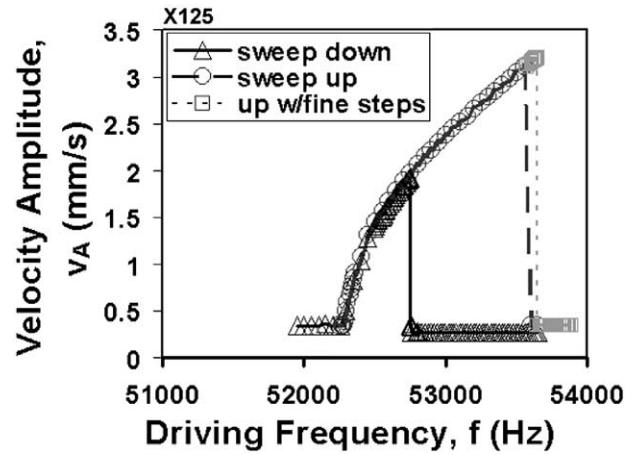


Fig. 13. Experimental data of frequency–amplitude curves as the input frequency is swept quasi-statically near first-order parametric resonance (twice the natural frequency and $\beta = 1$) at $V_A = 20$ V. The figure can be divided into three areas, I, II and III (refer Fig. 6 for the distinction). Point P is in the right transition curve ($\beta = 1 + \delta$) from area III to II and Q is in the left transition curve ($\beta = 1 - \delta$) from area II to I. Note there are two experimental responses in area III, corresponding to the two stable solutions. The points R and S are in region III where the response jumps from the large amplitude stable response to the trivial solution.

theorize that a larger frequency jump size perturbs the system enough to drive it out of the basin of attraction of the large response. Further discussion of this phenomenon is presented in Section 5.

5. Discussion

According to the analysis of nonlinear Mathieu equation, first-order parametric resonance as represented in the $\beta - \delta$ plane (which can be translated to $V_A - f$ coordinates) may be categorized into three areas, I, II and III (see Fig. 6(a)). The corresponding $A - B$ plane is shown in the same figure. In area I, only one trivial solution exists. As the frequency is changed quasi-statically, a bifurcation occurs at the left boundary ($\beta = 1 - \delta$). In area II, the trivial solution becomes unstable and simultaneously a stable sub-harmonic motion is born. This motion grows in amplitude as δ increases. In the right boundary ($\beta = 1 + \delta$), the unstable trivial solution becomes stable again and an unstable sub-harmonic motion is born. The stable sub-harmonic non-trivial solution born in area II also exists in area III.

The experimentally obtained displacements exactly verify all the characteristics expected from the analysis. Fig. 13 presents typical frequency response in the three zones described above. In area I, the response is very small, which corresponds to the stable trivial solution. In area II, a large response exists, corresponding to the stable non-trivial solution, while the unstable trivial solution cannot be found. In area III, one large and one small response can be found depending on the testing conditions. Analysis predicts that, depending on the initial displacement and velocity, the final

displacement converges to one of the two stable states. When sweeping frequency down, the initial value is small in area III and hence the trivial stable solution is obtained. But when sweeping the frequency up, in small step sizes, the response stabilizes at the non-trivial stable solution. For large step size sweeps, the response jumps to the trivial stable solution at a lower frequency. In Fig. 13, Point R shows this jump. It has been experimentally observed that, if the step size of the frequency sweep is made very small, the oscillator can be maintained in the large amplitude response to higher frequency (see RS in Fig. 13). From the theoretical analysis, it can be seen that the two stable solutions in region III have their own basins of attraction. This implies that the final state of the oscillator in this region depends on the initial condition of the oscillators. We theorize that the step size causes a perturbation in the initial conditions, thereby effecting the frequency at which the jump occurs. It is worthwhile to note here that, the difference in response between sweeping input frequency in either direction (up or down) is due to the bifurcations occurring at the boundaries.

The significant impact of this analysis and its experimental verification on the mass sensor is as follows. In order to be able to utilize the jump (sharp transition from trivial to non-trivial solution in β - δ plane), for the case of negative effective nonlinear parameter $\gamma_{3\text{eff}}$, we can use only one of the instability boundaries ($\beta = 1 + \delta$). The analysis predicts that the bifurcations will occur in the other instability boundary ($\beta = 1 - \delta$) where the system has a positive nonlinear parameter. In this paper, we limit the discussion to the case of negative effective nonlinear parameter $\gamma_{3\text{eff}}$. Fig. 14 shows a schematic of how the position of the instability boundary will change with change in mass. The two traces are simulations of the sharp boundary between a very small amplitude (trivial) response and a well-defined large amplitude response (Fig. 15), mapped for the reference oscillator and a sense oscillator with a mass change of 10^{-14} kg.

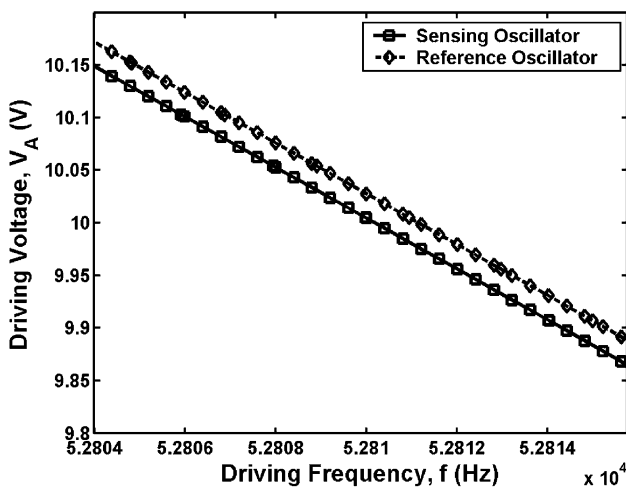


Fig. 14. Schematic of the effect of change in mass on the transition boundary between regions II and III. This is a simulation of the effect for a mass change of 10^{-14} kg.

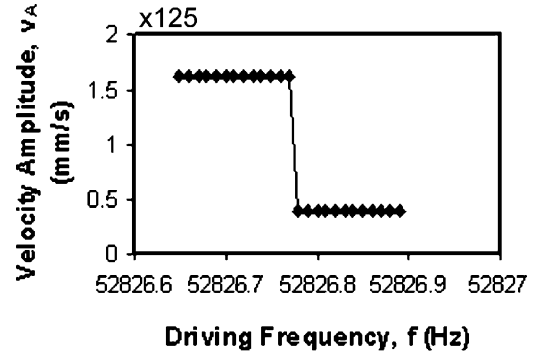


Fig. 15. Detail of the sharp transition from trivial solution to the non-trivial stable high amplitude solution as the drive frequency is changed quasi-statically from region III to region II.

It should be noted that, by varying the amplitude of the driving voltage, the effective nonlinear parameter can be tuned. The transition of this effective nonlinear parameter from positive to negative will switch the occurrence of the bifurcations from one side of the instability boundary to the other. This switch will be sharp and will occur at a well-defined V_A and can then be used to estimate the value of the cubic electrostatic stiffness with a good degree of accuracy (see Fig. 7). In the present experimental set up, this was not done as the required input voltage to change the effective cubic stiffness to be positive was estimated to be more than the breakdown voltage of the device oxide electrical insulator layer.

The presence of the cubic stiffness also results in a distinct advantage compared to that of the linear parametric mass sensor. In the case of the linear oscillator with parametric excitation, the transition boundaries separate regions of trivial solution from regions of exponentially growing sub-harmonic solutions. The presence of damping changes the rate of the exponential growth and alters the shape of the transition curve (from 'V' to 'U'), but does not limit the amplitude growth. This implies that a linear model cannot predict the experimentally observed amplitude. In any real system, the amplitude is finite and limited by factors not modeled, like the nonlinearity, or physical constraints. Thus, the advantage of modeling the cubic nonlinearity is that, we can estimate the final amplitude of the response inside the tongue.

Due to the cubic nonlinearity, the range of operation of the mass sensor is reduced, but the sensitivity of the sensor is not compromised. The above analysis and experimental verification illuminates the effect of the various design parameters on the sensor performance. This helps in developing good design rules. The sharp transitions can also be used as a self-calibrating tool to extract the system parameters with a good degree of confidence.

Additionally, from the analysis and experimental results, we note that the effect of the damping in the system is to shift the instability 'tongue' from one that looks like a 'V' to one that looks like a 'U' (see Fig. 6). This implies that there is a minimum input voltage above which the transition takes place (also see Fig. 12). The damping does not affect the

sensitivity of the mass sensor, but rather introduces a constraint in the input voltage signal amplitude, unlike the sensors based on simple harmonic oscillator resonance shifts. This is a very critical feature of the sensor since often the quality factor cannot be controlled with precision or made very large in test situations.

The response of the oscillator is not effected significantly due to process variations. The depth of the features is a parameter not easily controlled in the process conditions. This does not affect the design since the depth is not a design parameter and does not effect the natural frequency (the mechanical stiffness and the mass has the same dependence on the depth) to the first-order. We have published an analytical study of the effect of parameter variation due to process conditions on the frequency stability of lateral resonant oscillators elsewhere [31]. The stress and stress gradient effects are minimal in these deep etched single crystal silicon resonators of the design dimensions used in this work [32]. However, for implementations of such a mass sensor in other material systems, the ideas of Mehner et al. [33] could be used to model the stress and stress gradient effects in conjunction with our modeling approach.

6. Conclusion and future directions

In this paper, we present the modeling, analysis, and experimental verification of nonlinearity effects on an auto-parametric amplification based mass sensor. The effect of the cubic mechanical stiffness and electrostatic stiffness changes the dynamic behavior of the oscillator response when excited parametrically in parts of the parameter (frequency–amplitude of input voltage) space. This restricts the regions of operation of the mass sensor, but does not alter the sensitivity. The detailed modeling and analysis also serve as tools for design of the mass sensor. The sharp transition, which facilitates the high mass change detection, can also be used to estimate the system parameters with good degree of accuracy in the reference oscillator.

For use as a mass sensor, some more issues need to be taken into consideration. Understanding of the various sources of noises in the system is one main issue [34]. Also, we are investigating methods to activate the surface of the oscillator for selective reaction and perhaps increase the surface area using porous silicon. The effect of temperature on the frequency response of parametric resonance is another critical issue. To increase the sensitivity, the design and fabrication of a new oscillator with higher natural frequency is under progress.

Acknowledgements

The authors would like to thank Scott Adams for the device fabrication. This work is supported by NSF CAREER award #0093994.

References

- [1] L. Ruby, Applications of the Mathieu equation, *Am. J. Phys.* 64 (1996) 39–44.
- [2] J.A. Burns, More on pumping a swing, *Am. J. Phys.* 38 (1970) 920–921.
- [3] J.W.S. Rayleigh, R.B. Lindsay, *The Theory of Sound*, Dover Publications, New York, 1st American, 1945, pp.
- [4] K.L. Turner, S.A. Miller, P.G. Hartwell, N.C. Macdonald, S.H. Strogartz, S.G. Adams, Five parametric resonances in a microelectromechanical system, *Nature* 396 (1998) 149–152.
- [5] K.L. Turner, W. Zhang, Design and analysis of a dynamic MEM chemical sensor, in: *Proceedings of the 2001 American Control Conference*, Arlington, VA, USA, 25–27 June 2001, pp. 1214–1218.
- [6] J.P. Raskin, A.R. Brown, B. Khuri-Yakub, G.M. Rebeiz, A novel parametric-effect MEMS amplifier, *J. Microelectromech. Syst.* 9 (2000) 528–537.
- [7] A. Olkhovets, D.W. Carr, J.M. Parpia, H.G. Craighead, Non-degenerate nanomechanical parametric amplifier, in: *Proceedings of the 14th IEEE International Conference on Micro Electro Mechanical Systems*, Interlaken, Switzerland, 21–25 January 2001, pp. 298–300.
- [8] M.K. Baller, H.P. Lang, J. Fritz, C. Gerber, J.K. Gimzewski, U. Drechsler, H. Rothuizen, M. Despont, P. Vettiger, F.M. Battiston, J.P. Ramseyer, P. Fornaro, E. Meyer, H.J. Guntherodt, A cantilever array-based artificial nose, in: *Proceedings of the International Conference on Scanning Probe Microscopy, Cantilever Sensors and Nanostructures*, Seattle, WA, USA, 30 May–1 June 1999, pp. 1–9.
- [9] T. Bachelis, R. Schafer, Microfabricated cantilever-based detector for molecular beam experiments, *Rev. Sci. Instrum.* 69 (1998) 3794–3797.
- [10] T.D. Stowe, K. Yasumura, T.W. Kenny, D. Botkin, K. Wago, D. Rugar, Attonewton force detection using ultrathin silicon cantilevers, *Appl. Phys. Lett.* 71 (1997) 288–290.
- [11] T. Kenny, Nanometer-scale force sensing with MEMS devices, *IEEE Sens. J.* 1 (2001) 148–157.
- [12] P. Mohanty, D.A. Harrington, M.L. Roukes, Measurement of small forces in micron-sized resonators, in: *Proceedings of the 22nd International Conference on Low Temperature Physics*, Espoo, Finland, 4–11 August 1999, pp. 2143–2144.
- [13] M. Cartmell, *Introduction to Linear, Parametric, and Nonlinear Vibrations*, Chapman & Hall, London, 1990, pp. xii, 242.
- [14] K.L. Turner, P.G. Hartwell, F.M. Bertsch, N.C. Macdonald, Parametric resonance in a microelectromechanical torsional oscillator, in: *ASME International Mechanical Engineering Congress and Exposition Proceedings of the Microelectromechanical Systems (MEMS)*, Anaheim, CA, USA, 15–20 November 1998, pp. 335–340.
- [15] R. Berger, C. Gerber, H.P. Lang, J.K. Gimzewski, Micromechanics: a toolbox for femtoscale science: towards a laboratory on a tip, in: *Proceedings of the International Conference on Micro- and Nanofabrication*, Glasgow, UK, 22–25 September 1996, pp. 373–379.
- [16] T. Thundat, P.I. Oden, R.J. Warmack, Microcantilever sensors, *Microscale Thermophys. Eng.* 1 (1997) 185–199.
- [17] T. Thundat, R.J. Warmack, G.Y. Chen, D.P. Allison, Thermal and ambient-induced deflections of scanning force microscope cantilevers, *Appl. Phys. Lett.* 64 (1994) 2894–2896.
- [18] B. Vu Thien, N. Garcia, A.L. Levanyuk, A mechanical nanosensor in the gigahertz range: where mechanics meets electronics, *Surf. Sci.* 301 (1994) L224–228.
- [19] R. Lifshitz, M.L. Roukes, Thermoelastic damping in micro- and nanomechanical systems, *Phys. Rev. B, Condens. Matter* 61 (2000) 5600–5609.
- [20] Z.J. Davis, G. Abadal, O. Kuhn, O. Hansen, F. Grey, A. Boisen, Fabrication and characterization of nanoresonating devices for mass detection, *J. Vac. Sci. Technol. B, Microelectron. Nanometer Struct.* 18 (2000) 612–616.

- [21] N.C. Macdonald, SCREAM microelectromechanical systems, *Microelectron. Eng.* 32 (1996) 49–73.
- [22] S.G. Adams, F.M. Bertsch, K.A. Shaw, N.C. Macdonald, Independent tuning of linear and nonlinear stiffness coefficients (actuators), *J. Microelectromech. Syst.* 7 (1998) 172–180.
- [23] ANSYS, Release 5.7.
- [24] COULOMB, Three-Dimensional Electrostatic Field Solver, Version 5.1 (2000).
- [25] R. Grimshaw, *Nonlinear Ordinary Differential Equations*, CRC Press, Boca Raton, FL, 1993, pp. viii, 328.
- [26] S. Evoy, D.W. Carr, L. Sekaric, A. Olkhovets, J.M. Parpia, H.G. Craighead, Nanofabrication and electrostatic operation of single-crystal silicon paddle oscillators, *J. Appl. Phys.* 86 (1999) 6072–6077.
- [27] M. Aikele, K. Bauer, W. Ficker, F. Neubauer, U. Prechtel, J. Schalk, H. Seidel, Resonant accelerometer with self-test, in: *Proceedings of the EUROSENSORS, 14th European Conference*, Copenhagen, Denmark, 27–30 August 2000, pp. 161–167.
- [28] R.H. Rand, *Lecture Notes on Nonlinear Vibrations*, Version 34a, Available online at <http://www.tam.cornell.edu/randdocs/>, 2000.
- [29] K.L. Turner, Multi-dimensional MEMS motion characterization using laser vibrometry, in: *Transducers'99 The 10th International conference on solid-state Sensors and Actuators*, Digest of Technical Papers, Sendai, Japan, 7–10 June 1999, pp. 1144–1147.
- [30] Polytec, *Vibrometer User's Manual* (1999).
- [31] L. Rong, B. Paden, K. Turner, MEMS resonators that are robust to process-induced feature width variations, in: *Proceedings of the 2001 IEEE International Frequency Control Symposium and PDA Exhibition*, Seattle, WA, USA, 6–8 June 2001, pp. 556–563.
- [32] M.T.A. Saif, N.C. Macdonald, Planarity of large MEMS, *J. Microelectromech. Syst.* 5 (1996) 79–97.
- [33] J.E. Mehner, L.D. Gabbay, S.D. Senturia, Computer-aided generation of nonlinear reduced-order dynamic macromodels. Part II. Stress-stiffened case, *J. Microelectromech. Syst.* 9 (2000) 270–278.
- [34] T.B. Gabrielson, Mechanical-thermal noise in micromachined acoustic and vibration sensors, *IEEE Trans. Electron Devices* 40 (1993) 903–909.

Biographies

Wenhua Zhang is currently a Ph.D. candidate in the department of Mechanical and Environmental Engineering at University of California, Santa Barbara. He received his master degree in plasma processing from Institute of Mechanics, Chinese Academy of Sciences in 1999. His research interests are in dynamics and characterization of MEMS.

Rajashree Baskaran is working towards her Ph.D. at University of California, Santa Barbara. She got her Master's degree in the field of theoretical and applied mechanics from Cornell University in 2000. Her research interests are in the field of studying nonlinear dynamics of micro electromechanical systems.

Kimberly Turner received her BS in mechanical engineering from Michigan Technological University in 1994, and her Ph.D. from Cornell University in 1999. She has been an Assistant Prof. of mechanical and environmental engineering at UC Santa Barbara since July 1999. She supervises seven graduate students, and three undergraduate researchers. Dr. Turner is the recipient of a 2001 NSF CAREER award. She is a member of many professional societies including ASME, IEEE, ASEE, SEM, and AVS.